

Exact and approximative imaging methods for photoacoustic tomography using an arbitrary detection surface

Peter Burgholzer* and Gebhard J. Matt

Department of Sensor Technology, Upper Austrian Research GmbH, Hafenstraße 47-51, 4020 Linz, Austria

Markus Haltmeier

Department of Computer Science, Universität Innsbruck, Technikerstr. 21a/2, 6020 Innsbruck, Austria

Günther Paltauf

Department of Physics, Karl-Franzens Universität Graz, Universitätsplatz 5, 8010 Graz, Austria

(Received 7 July 2006; revised manuscript received 20 November 2006; published 17 April 2007)

Two universal reconstruction methods for photoacoustic (also called optoacoustic or thermoacoustic) computed tomography are derived, applicable to an arbitrarily shaped detection surface. In photoacoustic tomography acoustic pressure waves are induced by illuminating a semitransparent sample with pulsed electromagnetic radiation and are measured on a detection surface outside the sample. The imaging problem consists in reconstructing the initial pressure sources from those measurements. The first solution to this problem is based on the time reversal of the acoustic pressure field with a second order embedded boundary method. The pressure on the arbitrarily shaped detection surface is set to coincide with the measured data in reversed temporal order. In the second approach the reconstruction problem is solved by calculating the far-field approximation, a concept well known in physics, where the generated acoustic wave is approximated by an outgoing spherical wave with the reconstruction point as center. Numerical simulations are used to compare the proposed universal reconstruction methods with existing algorithms.

DOI: [10.1103/PhysRevE.75.046706](https://doi.org/10.1103/PhysRevE.75.046706)

PACS number(s): 95.75.Mn, 42.30.Wb, 87.57.Ce, 43.35.+d

I. INTRODUCTION

Photoacoustic computed tomography, also known as optoacoustic or thermoacoustic tomography, is based on the generation of sound in a semitransparent medium by absorption of a pulsed electromagnetic wave. It is an imaging method for visualization of light-absorbing structures buried in turbid media with applications mainly in the diagnostics of biological tissue [1–3]. When a semitransparent sample is illuminated by a short pulse of electromagnetic radiation, such as light or radio waves, a spatial distribution of acoustic pressure inside the sample is generated by thermoelastic expansion, which induces the emission of acoustic waves. The generated initial pressure distribution is proportional to the volumetric density of the locally absorbed electromagnetic energy. In photoacoustic imaging the goal is to recover this absorption density inside the sample as a function of space from acoustic pressure signals measured outside the illuminated sample (photoacoustic inverse problem). The resulting imaging contrast is optical, whereas the imaging technique is mainly acoustic, thus combining the advantages of two important noninvasive imaging technologies: diffuse optical and ultrasonic imaging.

The purpose of the present study was to derive and compare two algorithms for the inverse photoacoustic problem in the case of an arbitrary detection surface. This is the surface over which the detectors receiving the acoustic signals are distributed or scanned during image acquisition. For spherical, cylindrical, and planar arrangements of detectors exact

inversion formulas have been reported, either in the frequency domain [4–7] or in the time domain [8–11]. In practical applications the detection surface may differ from those simple geometrical shapes. For instance, it may be advantageous that the detector surface follows as close as possible the shape of the imaged object in order to keep the propagation length of acoustic waves as small as possible, thereby minimizing the acoustic attenuation. In particular, the preferential attenuation of high frequencies limits the achievable spatial resolution. Xu and Wang have applied the time reversal method [12] for an arbitrary closed detection surface. They presented a formal back-projection solution with the Green's function subject to the homogeneous Dirichlet boundary condition on the detection surface. For an arbitrary surface no analytic expression for this Green's function exists. Therefore, they approximated it by the Green's function in free space resulting in their universal back-projection formula, which is exact for a spherical or cylindrical detection surface [11]. In this article we propose a numerical method to calculate directly the time reversed field by retransmitting the measured pressure on the detection surface in reversed temporal order. This results in a universal and exact image reconstruction method for an arbitrary closed detection surface. This method is compared to a universal far-field approximation that turns out to be identical to a modified back-projection formula derived by Xu and Wang [8,9] for spherical, cylindrical, and planar detection surfaces from Fourier-domain reconstruction formulas. The derivation of the far-field approximation presented here does not depend on the actual shape of the detection surface, proving that the algorithm is suitable for an arbitrary arrangement of detectors as well.

*Electronic address: peter.burgholzer@uar.at

Among the challenges a practically useful reconstruction algorithm has to deal with is the actual physical characteristics of the detector. Both the detector bandwidth and size have an influence on the imaging resolution. Applying a reconstruction method that assumes point receivers to signals measured with a detector with finite size leads to blurring of the image. Only in the case of a planar detection surface this blurring can be reduced by use of a deconvolution procedure [6]. Recently it has been shown that also with large-aperture detectors which in at least one dimension exceed the size of the imaged object high-resolution imaging is possible by applying special reconstruction algorithms [13,14]. If the acoustic pressure outside the illuminated sample is measured with such a large-aperture detector, called the “integrating detector,” the signal at a certain time is given by an integral of the generated acoustic pressure distribution where the integration area is determined by the shape of the detector. For example, a planar detector measures the projections of the initial pressure distribution over planes parallel to the detector plane, which is the Radon transform of the initial pressure distribution [15]. Stable and exact three-dimensional imaging with a planar integrating detector requires measurements in all directions of space and so the receiver plane has to be rotated to cover the entire detection surface. We have recently presented a simpler setup for exact imaging that requires only a single rotation axis and uses the fragmentation of the area detector into an array of line detectors perpendicular to this rotation axis [13,16,17]. Integration of the acoustic waves along the linear detector leads to a two-dimensional problem, where the detection surface is reduced to a curve. From data taken at a certain orientation of the linear detector a linear projection of the initial pressure distribution can be reconstructed. Multiple projections in different directions are used to reconstruct the original source via the inverse Radon transform. Only for an infinitely long straight detection line [13,18] and a circle [14,19,20] exact reconstruction algorithms for the two-dimensional problem are available. The time reversal method presented in this study, since it is based on the finite difference solution of the wave equation, can easily be adapted to the two-dimensional problem.

Two main problems encountered in an *in vivo* application of photoacoustic imaging, such as breast tomography are limited view data acquisition (i.e., the detection surface is not closed) [21] and the acoustic heterogeneity of the imaged object [22]. It turns out that the far field reconstruction is better suited for limited view data, whereas the time reversal method can take into account the effect of locally varying sound velocity and the effect of frequency dependent acoustic attenuation by changing the sign of the loss term (first or third order in time) in the wave equation. Using the far-field approximation to calculate the missing data from limited view data and then the time reversal method for reconstruction combines the advantages of both methods.

This article is organized as follows. In Sec. II photoacoustic tomography is briefly reviewed and the time reversal method is derived. The universal far-field inversion is described in Sec. III, followed by numerical simulations to compare and combine it with the time reversal method and also with reconstruction methods reported by Kruger *et al.*

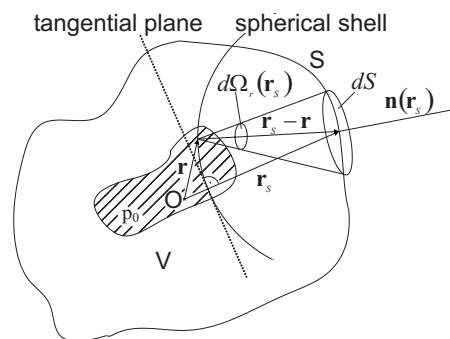


FIG. 1. Illustration of photoacoustic tomography. A pointlike detector at position \mathbf{r}_s scans across a closed surface S enclosing the object in the volume V . In the exact solution [as shown in Eq. (8)] the initial pressure distribution is integrated over spherical shells. In the far-field approximation the initial pressure distribution is integrated over planes shown as a dotted line. $d\Omega_r(\mathbf{r}_s)$ is the solid angle for a detector surface element dS at \mathbf{r}_s with normal vector $\mathbf{n}(\mathbf{r}_s)$ pointing outside the surface.

[23], Finch *et al.* [10], and Xu and Wang [11]. Finally, in Sec. V some conclusions and an outlook on future work are given.

II. PHOTOACOUSTIC TOMOGRAPHY BY TIME REVERSAL

Short laser pulses absorbed in a semitransparent object generate an initial pressure distribution $p_0(\mathbf{r}) = \Gamma W(\mathbf{r})$ proportional to the volumetric density $W(\mathbf{r})$ of the locally absorbed electromagnetic energy and the Grüneisen-parameter Γ . The induced pressure field at position \mathbf{r} and time t is denoted by $p(\mathbf{r}, t)$ and solves the inhomogeneous wave equation with a temporal Dirac delta function as source term [24]

$$\left(\frac{\partial^2}{\partial t^2} - c^2 \Delta \right) p(\mathbf{r}, t) = \frac{\partial}{\partial t} p_0(\mathbf{r}) \delta(t), \quad (1)$$

where Δ is the Laplacian with respect to the spatial variable \mathbf{r} and c is the sound velocity. The inverse photoacoustic problem is to reconstruct the initial pressure distribution p_0 from a set of data measured with detectors on a surface S outside the object (see Fig. 1).

Time reversal is based on the invariance of the wave equation under the transform $t \rightarrow -t$. This property is used in many practical applications, such as undersea communications, hydrodynamics, material analysis, and medicine [25]. Xu and Wang used time reversal to derive a universal back-projection formula [12], which is exact for a spherical and a cylindrical detection surface [11]. In this section we present a theoretically exact model-based time reversal algorithm to solve the photoacoustic imaging problem for an arbitrary closed detection surface.

A. Model based time reversal

Assume that p is a solution of Eq. (1) and let $T_0 > 0$ be large enough such that $p(\mathbf{r}, T_0) = 0$ inside the whole volume V enclosed by the surface S , see Fig. 1. T_0 can be chosen, e.g.,

as the maximal diameter of V divided by c . At time T_0 we start to rewind the time evolution and obtain the desired initial pressure distribution p_0 at time $2T_0$.

More precisely, the time reversal of p is defined as

$$p_{\text{tr}}(\mathbf{r}, t) := p(\mathbf{r}, 2T_0 - t), \quad T_0 \leq t \leq 2T_0. \quad (2)$$

According to the principle of Duhamel ([26], p. 81) the inhomogeneous wave Eq. (1) is equivalent to the homogeneous wave equation, together with the initial conditions $p(\mathbf{r}, 0) = p_0(\mathbf{r})$ and $(\partial p / \partial t)(\mathbf{r}, 0) = 0$. As the homogeneous wave equation is invariant under the transform $t \rightarrow -t$, $p_{\text{tr}}(\mathbf{r}, t)$ is a solution of the homogeneous wave equation with the initial conditions

$$p_{\text{tr}}(\mathbf{r}, T_0) = p(\mathbf{r}, T_0), \quad (\partial p_{\text{tr}} / \partial t)(\mathbf{r}, T_0) = -(\partial p / \partial t)(\mathbf{r}, T_0). \quad (3)$$

According to Eq. (2), the time reversal develops into the initial pressure distribution $p_0(\mathbf{r})$ at time $t = 2T_0$.

The homogeneous wave equation with the initial conditions Eq. (3) cannot be solved directly because the initial values $p_{\text{tr}}(\mathbf{r}, T_0)$ and $(\partial p_{\text{tr}} / \partial t)(\mathbf{r}, T_0)$ are only known inside of V , where both functions are zero. However as a substitute for the missing values $p_{\text{tr}}(\mathbf{r}, T_0)$ and $(\partial p_{\text{tr}} / \partial t)(\mathbf{r}, T_0)$ outside V , the measurements provide boundary values $p_{\text{tr}}(\mathbf{r}_S, t) = p(\mathbf{r}_S, 2T_0 - t)$ on the surface S . Consequently, the time reversal inside V satisfies the following initial boundary value problem (IBVP):

$$\left(\frac{\partial^2}{\partial t^2} - c^2 \Delta \right) p_{\text{tr}}(\mathbf{r}, t) = 0, \quad (\mathbf{r}, t) \in V \times [T_0, 2T_0] \quad (4a)$$

with the initial values

$$p_{\text{tr}}(\mathbf{r}, T_0) = (\partial p_{\text{tr}} / \partial t)(\mathbf{r}, T_0) = 0, \quad \mathbf{r} \in V \quad (4b)$$

and the boundary values

$$p_{\text{tr}}(\mathbf{r}_S, t) = p(\mathbf{r}_S, 2T_0 - t), \quad (\mathbf{r}_S, t) \in S \times [T_0, 2T_0]. \quad (4c)$$

The IBVP (4a)–(4c) is uniquely solvable, see, for example, Ref. [26], p. 83 ff. This is crucial since it guarantees that the time reversal p_{tr} can be found as the unique solution of Eqs. (4a)–(4c). Moreover, it implies that the knowledge of the evolved pressure outside of the closed detection surface is not necessary to determine the pressure inside of S , and the solution at the time $t = 2T_0$ gives an exact reconstruction of p_0 . This also holds in a discrete setting, as presented in the next subsection. Note that a similar IBVP using the n -dimensional velocity potential has been proposed by Finch *et al.* [10] (theorem 5).

For an arbitrary detection surface, no analytic solution of Eqs. (4a)–(4c) is known. The Kirchhoff-Helmholtz integral gives an explicit formula, but only if additionally to Eq. (4c) the normal derivative of $p_{\text{tr}}(\mathbf{r}, t)$ on S is given, see Appendix A. However, fast and stable numerical algorithms for solving Eqs. (4a)–(4c) based on finite difference approximations [27,28], spectral [29], or boundary integral methods [30] are well investigated. In the next subsection we propose an embedded boundary algorithm, where the pressure on S is forced to coincide with the measured pressure in reversed

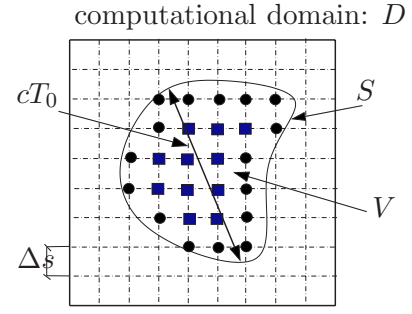


FIG. 2. (Color online) The region V is embedded into a cubic computational domain D , which is discretized by grid points with a step size of Δs . The interior points (squares) have all nearest neighbors inside V and the boundary points (circles) have at least one neighbor outside V .

temporal order. This implicitly takes the normal derivative of $p_{\text{tr}}(\mathbf{r}, t)$ into account and results in a universal and theoretically exact image reconstruction method for an arbitrary closed detection surface.

The main drawback of model based time reversal is that it applies only to surfaces enclosing the object to be imaged. Open surfaces, such as a hemisphere, are not included in our method. However, an approximate time reversal algorithm is obtained by setting the pressure on the inaccessible part of the boundary to zero or by using the far-field approximation [see Eq. (12) of the following section] to calculate this pressure.

B. Embedded boundary algorithm

In the following we described how to solve Eqs. (4a)–(4c) numerically. We assume that discrete measurement data taken at N_S different locations \mathbf{r}_S^m with $m \in \{0, \dots, N_S\}$ are available. As shown in Fig. 2, the volume V is embedded in a cuboidal domain D (the reason why the algorithm is called embedded boundary algorithm). For the sake of clarity of presentation we assume that $D = [-a, a]^3$ is a cube, where $2a$ is its side length.

The cubic domain D is discretized as Cartesian grid with grid points

$$\mathbf{r}^{\mathbf{n}} := -a(1, 1, 1) + \Delta s(n_1, n_2, n_3), \quad (5)$$

where $\mathbf{n} = (n_1, n_2, n_3) \in \{0, \dots, N\}^3$ are the spatial indices and $\Delta s = (2a)/N$ is the spatial step size. Solving Eqs. (4a)–(4c) numerically consists in calculating an approximation

$$p^{\mathbf{n}, k} \cong p_{\text{tr}}(\mathbf{r}^{\mathbf{n}}, T_0 + k\Delta t), \quad k \in \{0, \dots, N_t\} \quad (6)$$

to the true solution, evaluated at all grid points $\mathbf{r}^{\mathbf{n}} \in V$ and time instances $T_0 + k\Delta t$. Here and in the sequel Δt denotes the time step size. Our proposal, a hybrid embedded boundary method, based on finite difference approximation and nearest neighborhood interpolation, is outlined in the following.

In the first step all grid points in V are classified as interior points and boundary points: An interior point is a grid point $\mathbf{r}^{\mathbf{n}}$ in V such that all of its nearest neighbors are in V , whereas a boundary point is defined as a grid point $\mathbf{r}^{\mathbf{n}}$ in V that has at least one nearest neighbor outside V , see Fig. 2. For a bound-

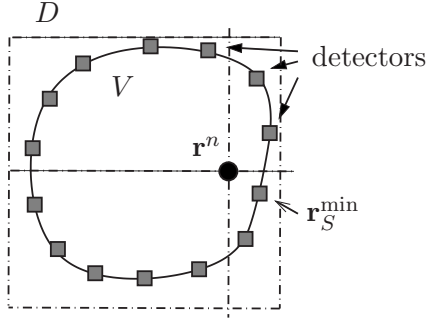


FIG. 3. The pressure at the boundary points is calculated by nearest neighborhood interpolation.

any point \mathbf{r}^n , $p^{\mathbf{n},k}$ is defined by nearest neighborhood interpolation using the given pressure on the boundary only. That is, we define

$$p^{\mathbf{n},k} := p(\mathbf{r}_S^{\min}, T_0 + k\Delta t), \quad (7a)$$

where \mathbf{r}_S^{\min} is the detector point with minimal distance to the boundary point \mathbf{r}^n , see Fig. 3.

Next it is described how to calculate $p^{\mathbf{n},k}$ for an interior point. This is done by approximating the temporal and spatial derivatives in Eq. (4a) with second order finite differences [27], leading to

$$\begin{aligned} \frac{1}{\Delta t^2} [p_{\text{tr}}(\mathbf{r}^n, t + \Delta t) - 2p_{\text{tr}}(\mathbf{r}^n, t) + p_{\text{tr}}(\mathbf{r}^n, t - \Delta t)] \\ \cong \frac{6c^2}{\Delta s^2} [\bar{p}_{\text{tr}}(\mathbf{r}^n, t) - p_{\text{tr}}(\mathbf{r}, t)]. \end{aligned}$$

Here $\bar{p}(\mathbf{r}^n, t)$ is the mean value of p over the 6 nearest neighbors of \mathbf{r}^n . Based on this approximation, we define $p^{\mathbf{n},k+1}$ recursively as

$$p^{\mathbf{n},k+1} := 2p^{\mathbf{n},k} - p^{\mathbf{n},k-1} + 6c^2 \frac{\Delta t^2}{\Delta s^2} (\bar{p}^{\mathbf{n},k} - p^{\mathbf{n},k}), \quad (7b)$$

where $\bar{p}^{\mathbf{n},k} = 1/6 \sum_{\mathbf{n}'} p^{\mathbf{n}',k}$ is the mean value of over all nearest neighbors of \mathbf{n} . The initial conditions (4b) are incorporated by setting

$$p^{\mathbf{n},0} = p^{\mathbf{n},1} = 0. \quad (7c)$$

The finite difference scheme (7a)–(7c) is the discrete analog of Eqs. (4a)–(4c). As in the continuous formulation, the discrete initial values and the boundary values allow for calculating $p^{\mathbf{n},k}$ at all grid points \mathbf{r}^n inside the surface without knowledge of the pressure on grid points outside the surface. The time discretization has to be chosen to satisfy the Courant-Friedrich-Lewy (CFL) condition $\Delta t \leq \Delta x / \sqrt{3}c$ [28]. Since the definition of the boundary points is independent of the spatial density of detection, the algorithm does not break down when decreasing the number of detector points. However, to keep the discretization error in Eq. (7a) small, the spatial density of detection is chosen to be higher than the density of the grid points \mathbf{r}^n .

In the following we estimate the numerical effort of the embedded boundary algorithm. We choose $\Delta t \sim \Delta x$, such that $N_t = O(N)$. Moreover, we assume that

$$V = \{\mathbf{r} \in \mathbb{R}^3 : \Phi(\mathbf{r}) > 0\}$$

is defined by some real valued function Φ . If, e.g., $\Phi(\mathbf{r}) = R^2 - |\mathbf{r}|^2$, then V is a ball of radius R . Consequently, the classification into boundary and interior points can be done by calculating $\Phi(\mathbf{r}^n)$ for all $(N+1)^3$ grid points, showing that $O(N^3)$ operations are required to classify all grid points. Moreover, the nearest neighborhood interpolation (7a) requires $O(N^3)$ operations. The most time consuming part is to solve the wave equation backwards, where we have to evaluate (7b) for N_t time steps. For fixed $k \in \{0, \dots, N_t - 1\}$, $O(N^3)$ operations are needed to calculate Eq. (7b). Therefore, performing the complete time reversal algorithm requires $O(N^4)$ operations.

It is remarkable, that the frequently used filtered back-projection, or delay and sum, algorithms require $O(N^5)$ operations (see Ref. [31] and compare also with Sec. III) which is one order higher than time reversal with finite differences. Therefore, the embedded boundary method is a considerable fast alternative, even if exact back-projection formulas are known for special detection surfaces.

III. UNIVERSAL FAR-FIELD INVERSION

The forward problem, the calculation of the pressure transients at $\mathbf{r}_S \in S$ (location of the detector, see Fig. 1) from the initial pressure distribution, can be solved using the Green's function in free space [32], leading to the Poisson integral

$$\begin{aligned} p(\mathbf{r}_S, t) &= \frac{1}{4\pi c} \frac{\partial}{\partial t} \int_{|\mathbf{r}_S - \mathbf{r}| = ct} \frac{p_0(\mathbf{r})}{|\mathbf{r}_S - \mathbf{r}|} dS \\ &= \frac{1}{4\pi} \frac{\partial}{\partial t} \left(t \int_{|\mathbf{r}_S - \mathbf{r}| = ct} p_0(\mathbf{r}) d\Omega \right). \end{aligned} \quad (8)$$

The first integral in Eq. (8) is a surface integral over a sphere with radius ct and center \mathbf{r}_S . It can be transformed into an integral over the solid angle $d\Omega$, where $d\Omega = dS/(ct)^2$ is the solid angle element with respect to \mathbf{r}_S . Taking the Fourier transform in time t and denoting $k = \omega/c$ we get for the detected pressure at position \mathbf{r}_S in the frequency-domain

$$P(\mathbf{r}_S, \omega) = -\frac{ik}{4\pi c} \int_{\mathbb{R}^3} p_0(\mathbf{r}) \frac{e^{ik|\mathbf{r}_S - \mathbf{r}|}}{|\mathbf{r}_S - \mathbf{r}|} d\mathbf{r}, \quad (9)$$

with $P(\mathbf{r}_S, \omega) := \int_{-\infty}^{\infty} p(\mathbf{r}_S, t) e^{i\omega t} dt$ and $p(\mathbf{r}_S, t) = 1/(2\pi) \int_{-\infty}^{\infty} P(\mathbf{r}_S, \omega) e^{-i\omega t} d\omega$.

A. Far-field approximation

If the detection radius $r_S := |\mathbf{r}_S|$ is much larger than the wavelengths of the photoacoustic waves that are useful for imaging (size of imaged structures), we can apply the far-field approximation $kr_S \gg 1$, a well known concept in acoustics [33]. In the particular far-field approximation (Fraunhofer approximation) $|\mathbf{r}_S - \mathbf{r}|$ in Eq. (9) is approximated by $r_S - \mathbf{r}(\mathbf{r}_S/r_S)$ in the exponent and by r_S in the denominator. Consequently,

$$P(\mathbf{r}_S, \omega) \cong -\frac{ik}{4\pi c} \int_{\mathbb{R}^3} p_0(\mathbf{r}) \frac{e^{ik(r_S - \mathbf{r} \cdot \hat{\mathbf{r}}_S)}}{r_S} d\mathbf{r}$$

$$= -\frac{ik}{4\pi c} \frac{e^{ikr_S}}{r_S} \int_{\mathbb{R}^3} p_0(\mathbf{r}) e^{-ik\mathbf{r} \cdot \hat{\mathbf{r}}_S} d\mathbf{r},$$

where we set $\hat{\mathbf{r}}_S := \mathbf{r}_S / r_S$. Defining $\mathbf{k} := k\hat{\mathbf{r}}_S$ and $\hat{p}_0(\mathbf{k}) := \int_{\mathbb{R}^3} p_0(\mathbf{r}) e^{-ik\mathbf{r} \cdot \hat{\mathbf{r}}_S} d\mathbf{r}$, it follows that

$$P(\mathbf{r}_S, \omega) \cong -\frac{ik}{c} \frac{e^{ikr_S}}{4\pi r_S} \hat{p}_0(\mathbf{k}). \quad (10)$$

In this approximation the pressure wave is described as an outgoing spherical wave with amplitude $\hat{p}_0(\mathbf{k})$ and Eq. (10) directly relates the one dimensional (temporal) Fourier transform of the measuring data $p(\mathbf{r}_S, t)$ with the spatial Fourier transform of the initial pressure p_0 in direction $\hat{\mathbf{r}}_S := \mathbf{r}_S / r_S$.

In the following we transform Eq. (10) into the time domain. We shall make use of the Fourier-slice theorem [31] for the classical Radon transform, which states that the one-dimensional Fourier transform evaluated at k of the projection orthogonal to $\hat{\mathbf{r}}_S$ is equal to the three-dimensional Fourier transform (of the same function) evaluated at $k\hat{\mathbf{r}}_S$. Taking this into account and applying the inverse one-dimensional Fourier transform to Eq. (10), yields

$$p(\mathbf{r}_S, t) \cong \frac{1}{4\pi r_S c} \frac{\partial}{\partial t} g(\hat{\mathbf{r}}_S, r_S - ct)$$

$$= \frac{1}{4\pi c} \frac{\partial}{\partial t} \left(\int_{\hat{\mathbf{r}}_S \cdot \mathbf{r} = r_S - ct} \frac{p_0(\mathbf{r})}{r_S} dS(\mathbf{r}) \right). \quad (11)$$

Here $g(\hat{\mathbf{r}}_S, r_S - ct)$, the integral of p_0 over the plane with normal vector $\hat{\mathbf{r}}_S$ and distance $r_S - ct$ from the origin, is the classical three-dimensional Radon transform of p_0 [31]. It is worthwhile to compare the far-field approximation in the time-domain with the exact solution: In Eq. (8) the initial pressure is integrated over spherical shells, whereas in Eq. (11) it is integrated over a planar surface, as indicated by the dotted line in Fig. 1.

Using Eq. (11) and the symmetry properties of the Radon transform, it follows that

$$p(\mathbf{r}_-, t) \cong -\frac{r_S}{r_-} p\left(\mathbf{r}_S, \frac{r_S + r_-}{c} - t\right), \quad (12)$$

where \mathbf{r}_- is a point on the detection surface opposite to \mathbf{r}_S . Therefore, in the far-field approximation, the pressure field on one side of the detection surface is proportional to the time reversed field on the opposite side. This will be used in the next subsection to obtain an inversion formula if the object is not fully enclosed by the detection surface (limited angle).

B. Far-field inversion

Xu and Wang [8,9] derived approximate reconstruction formulas, separately for spherical, cylindrical, and planar detection surfaces, by using series expansions adapted to these surfaces. In this subsection we show that the far-field approximation (10) allows us to extend their so-called ‘‘modi-

fied back-projection formula’’ to arbitrary closed detection surfaces, in a uniform treatment. Moreover, we show that the formula also holds in a limited data situation, where the detection surface covers only a 2π solid angle.

Based on Eq. (10) and, for the moment, assuming a closed surface S , the photoacoustic inverse problem can be solved as follows: First, calculate the temporal Fourier transform $P(\mathbf{r}_S, \omega)$ of the measured data $p(\mathbf{r}_S, t)$ for all detector positions \mathbf{r}_S . Second, solve Eq. (10) for $\hat{p}_0(\mathbf{k})$ and finally apply the inverse Fourier transform to reconstruct $p_0(\mathbf{r})$. This lengthy but straightforward calculation can be performed directly in the time domain. Taking into account the inversion Formula $p_0 = (1/8\pi^2) \int_S g''(\hat{\mathbf{r}}_S, \mathbf{r} \cdot \mathbf{r}_S) d\Omega(\hat{\mathbf{r}}_S)$ for the classical Radon transform ([31], p. 20), Eq. (11) implies

$$p_0(\mathbf{r}) \cong -\frac{1}{2\pi c} \int_S r_S \left. \frac{\partial p(\mathbf{r}_S, t)}{\partial t} \right|_{ct=r_S - \mathbf{r} \cdot \hat{\mathbf{r}}_S} d\Omega_0(\hat{\mathbf{r}}_S). \quad (13)$$

Here $d\Omega_0(\hat{\mathbf{r}}_S) := \mathbf{n}(\mathbf{r}_S) \cdot \hat{\mathbf{r}}_S dS / r_S^2$ is the solid angle of the surface area element dS seen from the origin and $\mathbf{n}(\mathbf{r}_S)$ denotes the normal vector at \mathbf{r}_S pointing outside the surface S , see Fig. 1.

It can be shown that Eq. (13) is exact for any rotationally symmetric initial pressure distribution with the origin \mathbf{O} as rotation center. Therefore, the far-field approximation is still a good approximation if a small object is placed near the origin \mathbf{O} . As we have no restrictions about the shape of the detection surface, any reconstruction point \mathbf{r} inside V can be taken as origin of new shifted coordinates. Equation (13) for the new origin at \mathbf{r} , leads to

$$p_0(\mathbf{r}) \cong -\frac{1}{2\pi c} \int_S |\mathbf{r}_S - \mathbf{r}| \left. \frac{\partial p(\mathbf{r}_S, t)}{\partial t} \right|_{ct=|\mathbf{r}_S - \mathbf{r}|} d\Omega_{\mathbf{r}}(\mathbf{r}_S)$$

$$= -\frac{1}{2\pi} \int_S t \left. \frac{\partial p(\mathbf{r}_S, t)}{\partial t} \right|_{ct=|\mathbf{r}_S - \mathbf{r}|} d\Omega_{\mathbf{r}}(\mathbf{r}_S). \quad (14)$$

Here $d\Omega_{\mathbf{r}}(\mathbf{r}_S)$ denotes the solid angle element corresponding to a detector surface element dS when viewed from \mathbf{r} , which can be represented analytically as $\frac{dS}{|\mathbf{r}_S - \mathbf{r}|^2} \left[\frac{\mathbf{r}_S - \mathbf{r}}{|\mathbf{r}_S - \mathbf{r}|} \cdot \mathbf{n}(\mathbf{r}_S) \right]$ $\cong \frac{dS}{|\mathbf{r}_S - \mathbf{r}|^2} \left[\frac{\mathbf{r}_S}{r_S} \cdot \mathbf{n}(\mathbf{r}_S) \right]$. Equation (14) generalizes the approximation derived by Xu *et al.* [8,9] for spherical, cylindrical, and planar geometry. For a spherical detection surface a similar far-field approximation was derived by Kruger *et al.* [23] using dS/r_S^2 instead of $d\Omega_{\mathbf{r}}$.

In real life measurements, due to practical constraints, the detection surface may not enclose the sample. For example, it is only possible to use a half-spherical measurement surface to image a human breast. However, in this case, the solid angle of the hemisphere with respect to any location inside the breast is always larger than 2π . It is theoretically known [34], that any singularity of p_0 inside this volume, such as a jump of p_0 along a surface, is visible in such data. Therefore, any detection surface which covers a solid angle larger than 2π is sufficient for stable image reconstruction. This means it is possible, at least, in principle, to reconstruct p_0 without blurring and undesirable amplification of noise. And in fact, using Eq. (11) and the symmetry properties of the classical Radon transform, it follows that

$$p_0(\mathbf{r}) \cong -\frac{1}{\pi} \int_{S_r^+} t \left. \frac{\partial p(\mathbf{r}_S, t)}{\partial t} \right|_{ct=|\mathbf{r}_S-\mathbf{r}|} d\Omega_r(\mathbf{r}_S), \quad (15)$$

where S_r^+ is a subset of S such that $\{\mathbf{r}_S - \mathbf{r} : \mathbf{r}_S \in S_r^+\}$ covers a 2π solid angle.

C. Numerical implementation

The inverse far-field approximation (14) is implemented using a discrete filtered back-projection algorithm with linear interpolation. We assume that the surface S is parameterized as $\mathbf{r}_S = \mathbf{r}_S(u, v)$. In this case, Eq. (14) can be written as

$$p_0(\mathbf{r}) \cong \frac{1}{2\pi} \int \int_{u,v} t \left. \frac{\partial p(\mathbf{r}_S, t)}{\partial t} \right|_{ct=|\mathbf{r}_S-\mathbf{r}|} d\Omega_r(u, v), \quad (16)$$

$$d\Omega_r(u, v) := \frac{G(u, v) du dv}{|\mathbf{r}_S - \mathbf{r}|^2} \left[\mathbf{n} \frac{\mathbf{r}_S - \mathbf{r}}{|\mathbf{r}_S - \mathbf{r}|} \right],$$

where $G(u, v)$ is the Jacobian determinant

$$G(u, v) = \left[\det \begin{pmatrix} \left| \frac{\partial \mathbf{r}_S}{\partial u} \right|^2 & \frac{\partial \mathbf{r}_S}{\partial u} \cdot \frac{\partial \mathbf{r}_S}{\partial v} \\ \frac{\partial \mathbf{r}_S}{\partial u} \cdot \frac{\partial \mathbf{r}_S}{\partial v} & \left| \frac{\partial \mathbf{r}_S}{\partial v} \right|^2 \end{pmatrix} \right]^{1/2},$$

which can be calculated straight forward for any surface. If, for example, S is a sphere of radius R , then $u = \theta$ and $v = \varphi$ are spherical coordinates and $G = \sin \theta$.

Assuming that $\mathbf{r}_S^m = \mathbf{r}_S(u^m, v^m)$, Eq. (16) is discretized as follows: first, $t \partial p / \partial t(\mathbf{r}_S^m, t)$ is approximated with second order finite differences (filtering step) and extended to a continuous function $q(\mathbf{r}_S^m, \cdot)$ using linear interpolation. Second, the surface integral in Eq. (16) is evaluated with the trapezoidal rule, leading to

$$p_0(\mathbf{r}) \cong -\frac{1}{2\pi} \sum_{m=0}^{N_S} q(\mathbf{r}_S^m, |\mathbf{r} - \mathbf{r}_S^m|) \Delta\Omega^m(\mathbf{r}), \quad (17)$$

$$\Delta\Omega^m(\mathbf{r}) = \frac{G(u^m, v^m) \Delta u \Delta v}{|\mathbf{r}_S^m - \mathbf{r}|^2} \left[\mathbf{n}(u^m, v^m) \frac{\mathbf{r}_S^m - \mathbf{r}}{|\mathbf{r}_S^m - \mathbf{r}|} \right].$$

Here $\mathbf{r} = \mathbf{r}^{(n_1, n_2, n_3)}$ with $n_1, n_2, n_3 \in \{0, \dots, N\}$ are the reconstruction points on a uniform lattice including V and $\Delta u, \Delta v$ are the discretization in u, v , respectively. The numerical effort of the filtered back-projection algorithm is $O(N^3 N_S)$, since for all $(N+1)^3$ reconstruction points we have to sum over all transducer locations. Under the reasonable assumption $N_S \sim N^2$, this is equal to $O(N^5)$.

IV. SIMULATION RESULTS AND DISCUSSION

In this section numerical studies of an irregular detection surface that has the shape of a three-dimensional star, the shape of a head phantom (MRI data from MATLAB), as well as for a cubic and a spherical detection surface are presented. The cubic detection surface is also an example of an irregular

detection surface with edges and corners but is numerically simple to handle.

For the spherical detection surface exact analytical reconstruction formulas are reported: the universal back-projection formula from Xu and Wang [11,12], as well as the inversion formulas given by Finch *et al.* [10], which we combined to an exact and compact spherical inversion formula (see Appendix B)

$$p_0(\mathbf{r}) = -\frac{1}{2\pi r_0 c} \int_{|\mathbf{r}_S|=r_0} \left. \frac{\partial p(\mathbf{r}_S, t)}{\partial t} \right|_{ct=|\mathbf{r}_S-\mathbf{r}|} dS$$

$$= -\frac{r_0}{2\pi c} \int_{|\mathbf{r}_S|=r_0} \left. \frac{\partial p(\mathbf{r}_S, t)}{\partial t} \right|_{ct=|\mathbf{r}_S-\mathbf{r}|} d\Omega, \quad (18)$$

where the solid angle element $d\Omega = dS / (r_0)^2$ corresponds to a detection surface element dS viewed from the center of the detection sphere with radius r_0 . It simply states that the initial pressure p_0 can be reconstructed as the integral of the time derivative of the time retarded pressure over the spherical detection surface S enclosing the object. Moreover, the first photoacoustic inversion formula in 1995 by Kruger *et al.* [23] (see Sec. III B) was derived for a spherical detection surface.

In our numerical studies shown in Figs. 4–6 these methods are compared with the far-field approximation and the time reversal method for an irregular detection surface (star), a cubic, and a spherical detection surface, respectively. As initial pressure distribution we choose the Defrise phantom p_0 . It consists of five thin ellipsoids rotated around the horizontal axis $\mathbf{e}_1 := (1, 0, 0)$, see the dashed line in Fig. 4(a) and therefore contains high and low spatialfrequency components and is well suited to test tomographic image reconstruction algorithms. For more details on the Defrise phantom consult [35]. The generated waves were simulated via a decomposition of $p(x, t)$ into plane waves (Fourier method) according to Eqs. (3) and (4) in Köstli *et al.* [24]. In order to preclude possible inverse crime, the spatial discretization numbers for data simulation and image reconstruction are chosen to be relatively prime.

As it can be seen in Figs. 4(b) and 5(b) the far-field approximation has small deviations from the initial Defrise profile. Only near the detection surface, where the initial pressure is zero, additional features with small amplitude arise. A similar result gives the universal back-projection formula [11] in Figs. 4(c) and 5(c) for the star surface and the cubic detection surface, respectively. The time reversal method, as presented in Sec. III, is theoretically exact for arbitrary geometry and its implementation with the embedded boundary method gives very accurate reconstruction also near the detection surface [see Figs. 4(d) and 5(d)].

The far-field approximation in Fig. 6(a) used by Kruger *et al.* [23], is accurate near the center of the spherical detection surface but overestimates the initial pressure distribution close to the surface S (see also Ref. [35], Sec. 3.4). If the reconstructed structures are small compared to the radius of the detection surface, the far-field approximation described in Sec. [3] gives good results in the whole region enclosed by the detection surface. For the Defrise phantom consisting

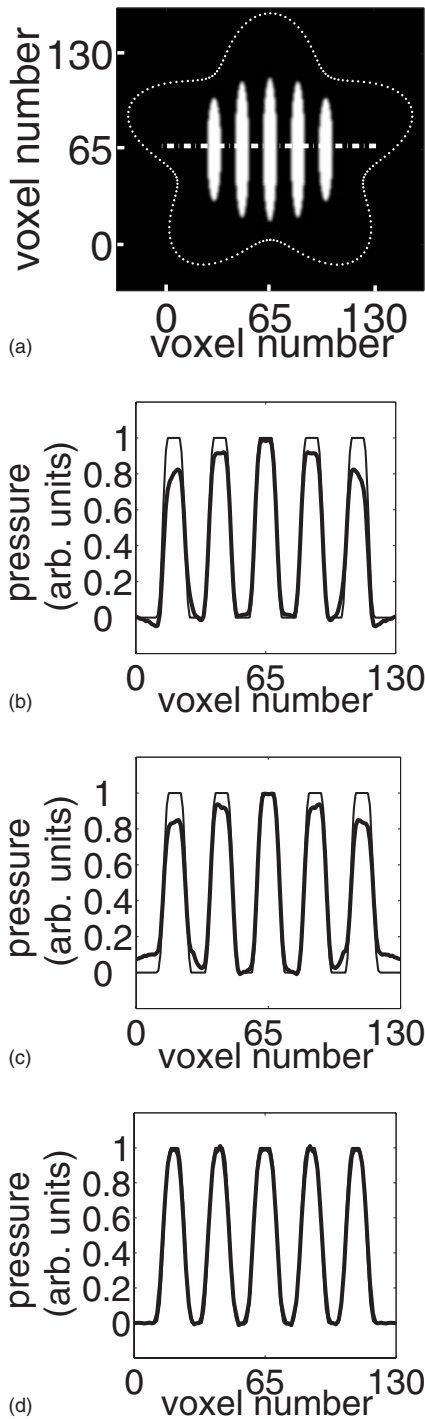


FIG. 4. Reconstruction profiles of the Defrise phantom. (a) Cross section of the Defrise phantom which consists of five thin ellipsoids rotated on the horizontal axis (dashed line) and an irregular detection surface (three-dimensional star); the pressure units are arbitrary and the diameter of the detection surface is approximately 130 voxels. Reconstruction profiles for (b) far-field approximation, (c) universal back-projection, and (d) time reversal method along the horizontal line of the Defrise phantom.

of the five ellipsoids altogether this assumption is not valid. This results in the underestimated and even negative pressure values near the detection surface as shown in Fig. 6(b). The universal back-projection formula and the spherical inver-

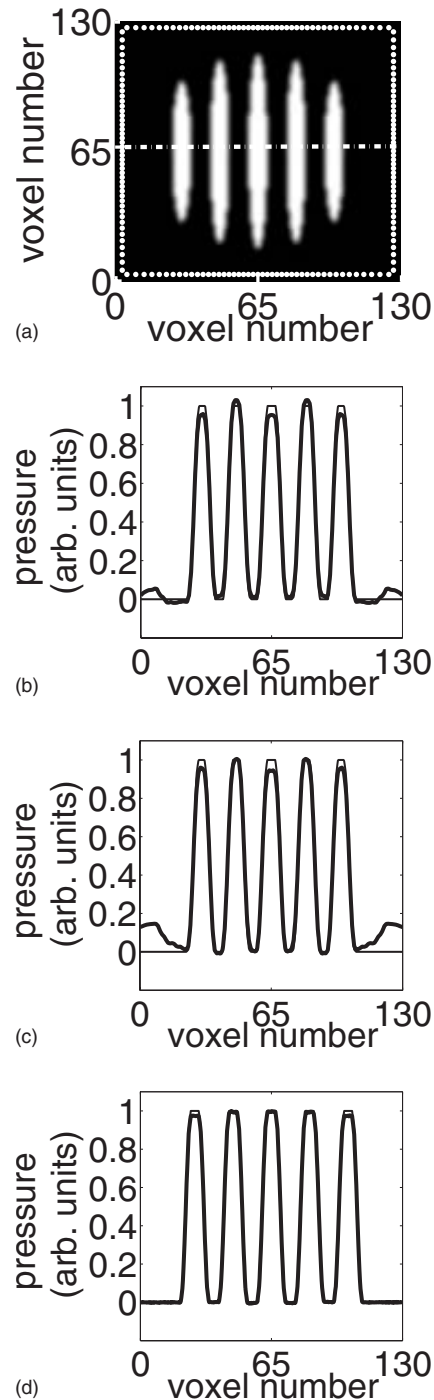


FIG. 5. Reconstruction profiles of the Defrise phantom. (a) Cross section of the Defrise phantom which consists of five thin ellipsoids rotated on the horizontal axis (dashed line) and a cubic detection surface (square); the pressure units are arbitrary. Reconstruction profiles for (b) far-field approximation, (c) universal back-projection, and (d) time reversal method along the horizontal line of the Defrise phantom.

sion formula of Eq. (18) are exact for a spherical detection surface and give excellent results [see Figs. 6(c) and 6(d), respectively]. The time reversal method is not included in Fig. 6 since it gives the same accurate result as in the case of the cubic surface presented in Fig. 5(d).

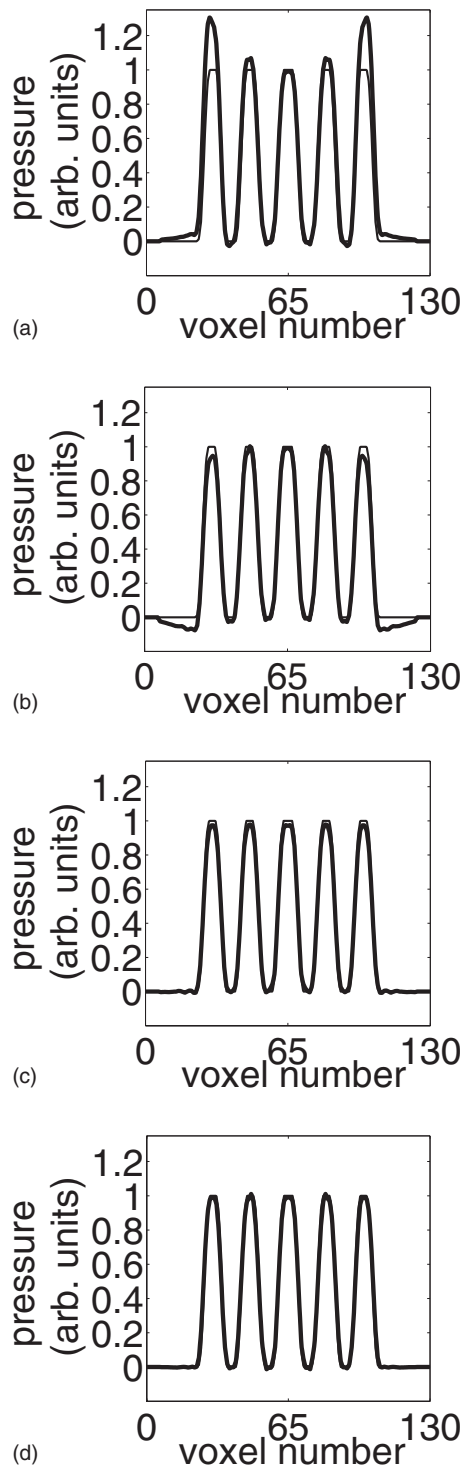


FIG. 6. Reconstruction profiles of the Defrise phantom in a spherical arrangement of pointlike detectors; pressure units are arbitrary; diameter of detection surface: 130 voxels. Reconstruction profiles for (a) Kruger approximation, (b) far-field approximation, (c) universal back-projection, and (d) spherical inversion formula (18), along the horizontal line of the Defrise phantom.

To demonstrate how the time reversal method can be applied also to open detection surfaces the pressure on the inaccessible part of the detection surface is set to zero [see Fig. 7(c)] or calculated by the far-field approximation Eq. (12)

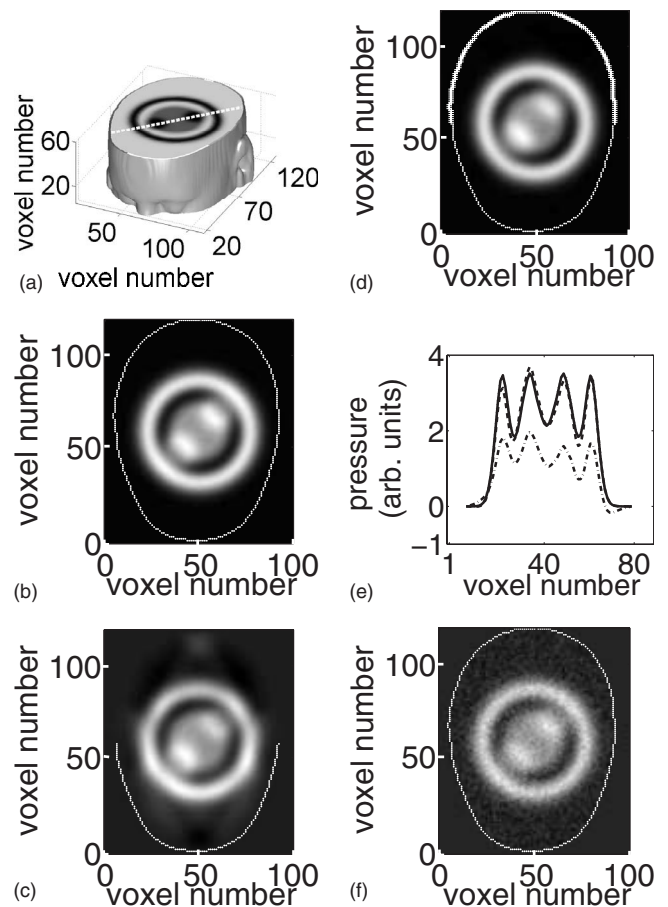


FIG. 7. Time reversal reconstruction of a phantom consisting of a superposition of spheres enclosed by an arrangement of pointlike detectors on the surface of a head phantom. (a) Horizontal cross-sectional view through initial data in head phantom. The white dashed line indicates where in (e) the reconstruction profile is shown. (b) Reconstructed cross-sectional view. (c) Reconstructed cross-section for limited view data. “Measurement data” on the back of the head is set to zero. (d) Reconstructed cross-section for limited view data. Missing data is calculated by Eq. (12) (far-field approximation). (e) Reconstruction profiles for the reconstruction images shown in (b) solid line, (c) dash dotted line, and (d) dashed line. The reconstruction profile for the enclosing head detection surface overlaps with initial data (solid line). (f) Cross-sectional view if 20% noise are added to the pressure on the detection surface before running the reconstruction.

[see Fig. 7(d)]. The reconstructed cross-sectional view for the whole head phantom as detection surface enclosing the initial pressure distribution is shown in Fig. 7(b). The initial pressure distribution is a superposition of spheres with a “Gaussian surface” to avoid discontinuities in pressure data [cross-sectional view in Fig. 7(a)]. For this initial pressure the pressure on the detection surface as a function of time can be calculated analytically (more details in Ref. [17]). For a quantitative comparison the reconstruction profiles along the white dashed line are shown in Fig. 7(e). To indicate the low noise sensitivity of the time reversal method 20% noise has been added to the analytically calculated pressure on the detection surface before running the reconstruction. The

cross-sectional view in Fig. 7(f) shows that even the two smaller spheres can be recognized clearly at that noise level.

V. CONCLUSIONS AND OUTLOOK

An inversion algorithm based on a far-field approximation and an exact algorithm using principles of time reversal have been derived for a photoacoustic tomography setup where the object is surrounded by an arbitrarily shaped detection surface that is formed by point receivers. Compared to existing reconstruction algorithms that are based on filtered back-projection the time reversal method implemented with a finite difference approach shows superior imaging accuracy. Moreover, it has been shown to be a considerable fast alternative to back-projection formulas. Even for an open detection surface, where the arrangement of receivers is arbitrarily shaped but does not fully enclose the object, the time reversal algorithm shows very accurate results by using the far-field approximation to calculate the pressure on a surface closing that detection surface.

Since time reversal actually inverses the acoustic wave propagation, it should allow for a compensation of the acoustic attenuation, thereby improving the imaging resolution that is limited by the frequency-dependent damping. To prevent high-frequency noise from growing exponentially, Fourier spectral methods [29] can be used. They utilize the Fourier transform to calculate the Laplacian and therefore allow for incorporating a cutoff frequency when calculating the time reversal. Another extension of the time reversal algorithm is the possibility of taking acoustic inhomogeneities into account, by replacing the sound velocity c in Eq. (7b) with a spatially varying coefficient c^n . As mentioned in the Introduction, future work will also be done using the time reversal method in two dimensions to reconstruct three-dimensional images with integrating line detectors.

ACKNOWLEDGMENTS

This work has been supported by the Austrian Science Fund (FWF), Project No. P18172-N02. Additionally, the work of M.H. has been supported by the FWF, Project No. Y123-INF. The authors wish to thank Michael Aichinger (Upper Austrian Research) for his helpful advice.

APPENDIX A: KIRCHHOFF-HELMHOLTZ INTEGRAL

Transforming the homogeneous wave equation into the frequency domain delivers the homogeneous Helmholtz equation $(k^2 + \Delta)P(\mathbf{r}, \omega) = 0$, where $P(\mathbf{r}, \omega)$ is the Fourier transform of $p(\mathbf{r}, t)$ in the variable t and $k = \omega/c$. The outgoing (or diverging) Green's function $G_k^+(\mathbf{r}|\mathbf{r}_0) = \exp(-ik|\mathbf{r} - \mathbf{r}_0|)/(4\pi|\mathbf{r} - \mathbf{r}_0|)$ is the fundamental solution of the inhomogeneous Helmholtz equation

$$-(k^2 + \Delta)G_k^+(\mathbf{r}|\mathbf{r}_0) = \delta(\mathbf{r} - \mathbf{r}_0); \quad (\text{A1})$$

where δ denotes the three dimensional Dirac delta function and \mathbf{r}_0 is some source point in V . Let \mathbf{n} denote the outward

normal to S , P a solution of the homogeneous Helmholtz equation and $G := G_k^+(\mathbf{r}|\mathbf{r}_0)$, then from the second Green's formula one gets

$$\int_S (-P \nabla G + G \nabla P) \cdot \mathbf{n} dS = \int_V (-P \Delta G + G \Delta P) d^3 r_0 = P(\mathbf{r}, \omega). \quad (\text{A2})$$

The surface integral on the left-hand side of Eq. (A2) is called the Kirchhoff-Helmholtz integral and shows, that any solution of the homogeneous Helmholtz equation (and hence any solution of the homogeneous wave) in V can be evaluated by integrating monopole—and dipole sources—respectively, $G \nabla P$ and $P \nabla G$ from Eq. (A2)—over the surface S .

If $G_k^{(V)}(\mathbf{r}|\mathbf{r}_S)$ denotes the diverging Green's function in V subject to homogeneous Dirichlet boundary conditions [that is $G_k^{(V)}$ satisfies Eq. (A1) in V and vanishes on S] then Eq. (A2) holds also true with $G = G_k^{(V)}$ [32]. In this case the monopole term in the Kirchhoff-Helmholtz integral will not contribute because $G_k^{(V)}$ is zero on S . By using the Fourier convolution theorem the resulting equation is transformed back into the time domain, leading to [Ref. [12], Eq. (13)]

$$p_0(\mathbf{r}) = - \int_S \left(\int_{T_0}^{2T_0} p_{\text{tr}}(\mathbf{r}_S, t) \nabla g_k^{(V)}(\mathbf{r}_S, t|\mathbf{r}, 2T_0) dt \right) \cdot \mathbf{n} dS, \quad (\text{A3})$$

where $g_k^{(V)}$ is the diverging Green's function in time domain of the wave equation subject to homogeneous Dirichlet boundary conditions on S .

Equation (A3) has a very important implication. The initial pressure can be obtained by retransmitting the measured pressure into a reflective cavity (formed by S), rather than retransmitting in free space itself. An insightful interpretation can be found in Ref. [12] [text following Eq. (13)].

APPENDIX B: COMPACT EXACT SPHERICAL INVERSION FORMULA

In three space dimensions, the first two n -dimensional inversion formulas given by Finch *et al.* [10] in theorem 3 read as follows:

$$p_0(\mathbf{r}) = - \frac{1}{2\pi r_0} \int_{|\mathbf{r}_S|=r_0} \frac{\partial^2 F(\mathbf{r}_S, \bar{t} = |\mathbf{r}_S - \mathbf{r}|)}{\partial \bar{t}^2} \frac{dS}{|\mathbf{r}_S - \mathbf{r}|}, \quad (\text{B1})$$

$$p_0(\mathbf{r}) = - \frac{1}{2\pi r_0} \int_{|\mathbf{r}_S|=r_0} \left. \frac{\partial [\bar{t} p(\mathbf{r}_S, t)]}{\partial \bar{t}} \right|_{\bar{t}=|\mathbf{r}_S - \mathbf{r}|/c} \frac{dS}{|\mathbf{r}_S - \mathbf{r}|}, \quad (\text{B2})$$

where $F(\mathbf{r}_S, \bar{t}) := \bar{t} \int_0^{\bar{t}} p(\mathbf{r}_S, t') dt'$. Subtracting these two formulas and taking into account the definition of F , gives Eq. (18).

- [1] X. Wang, Y. Pang, G. Ku, X. Xie, G. Stoica, and L.-H. Wang, *Nat. Biotechnol.* **21**, 803 (2003).
- [2] R. A. Kruger, W. L. Kiser, D. R. Reinecke, G. A. Kruger, and K. D. Miller, *Mol. Imaging* **2**, 113 (2003).
- [3] V. A. Andreev, A. A. Karabutov, S. V. Solomatin, E. V. Savateeva, V. Aleynikov, Y. V. Zhulina, R. D. Fleming, and A. A. Oraevsky, *Proc. SPIE* **3916**, 36 (2000).
- [4] S. J. Norton and M. Linzer, *IEEE Trans. Biomed. Eng.* **28**, 202 (1981).
- [5] K. P. Köstli, M. Frenz, H. Bebie, and H. P. Weber, *Phys. Med. Biol.* **46**, 1863 (2001).
- [6] Y. Xu, D. Feng, and L.-H. V. Wang, *IEEE Trans. Med. Imaging* **21**, 823 (2002).
- [7] Y. Xu, M.-H. Xu, and L.-H. V. Wang, *IEEE Trans. Med. Imaging* **21**, 829 (2002).
- [8] M.-H. Xu and L.-H. V. Wang, *IEEE Trans. Med. Imaging* **21**, 814 (2002).
- [9] M.-H. Xu, Y. Xu, and L.-H. V. Wang, *IEEE Trans. Biomed. Eng.* **50**, 1086 (2003).
- [10] D. Finch, S. Patch, and Rakesh, *SIAM J. Math. Anal.* **35**, 1213 (2004).
- [11] M. Xu and L. V. Wang, *Phys. Rev. E* **71**, 016706 (2005).
- [12] Y. Xu and L. V. Wang, *Phys. Rev. Lett.* **92**, 033902 (2004).
- [13] G. Paltauf, R. Nuster, M. Haltmeier, and P. Burgholzer, *Appl. Opt.* (to be published).
- [14] M. Haltmeier, O. Scherzer, P. Burgholzer, R. Nuster, and G. Paltauf, *Math. Models Methods Appl. Sci.* (to be published).
- [15] M. Haltmeier, O. Scherzer, P. Burgholzer, and G. Paltauf, *Inverse Probl.* **20**, 1663 (2004).
- [16] P. Burgholzer, C. Hofer, G. Paltauf, M. Haltmeier, and O. Scherzer, *IEEE Trans. Ultrason. Ferroelectr. Freq. Control* **52**, 1577 (2005).
- [17] P. Burgholzer, C. Hofer, G. Paltauf, and O. Scherzer, *Proc. SPIE* **5864**, 03 (2005).
- [18] K. P. Köstli and P. C. Beard, *Appl. Opt.* **42**, 1899 (2003).
- [19] S. J. Norton, *J. Acoust. Soc. Am.* **67**, 1266 (1980).
- [20] L. Kunyansky, eprint ArXiv:math.AP/0609341 (unpublished).
- [21] Y. Xu, L.-H. V. Wang, G. Ambartsoumian, and P. Kuchment, *Med. Phys.* **31**, 724 (2004).
- [22] Y. Xu and L.-H. V. Wang, *IEEE Trans. Ultrason. Ferroelectr. Freq. Control* **50**, 1134 (2003).
- [23] R. A. Kruger, P. Lui, Y. R. Fang, and C. R. Appledorn, *Med. Phys.* **22**, 1605 (1995).
- [24] K. P. Köstli, D. Frauchinger, J. Niederhauser, G. Paltauf, H. Weber, and M. Frenz, *IEEE J. Sel. Top. Quantum Electron.* **7**, 918 (2001).
- [25] M. Fink, *Phys. Today* **3**, 34 (1997).
- [26] L. C. Evans, *Partial Differential Equations* (American Mathematical Society, Providence, 1998).
- [27] A. R. Mitchell and D. F. Griffiths, *Finite Difference Method in Partial Differential Equations* (Wiley, New York, 1980).
- [28] B. Gustafsson, H.-O. Kreiss, and J. Olinger, *Time Dependent Problems and Difference Methods, Pure and Applied Mathematics* (Wiley, New York, 1995).
- [29] L. M. Trefethen, *Spectral Methods in Matlab* (SIAM, Philadelphia, 2000).
- [30] R. D. Ciskowski, *Boundary Methods in Acoustics* (Kluwer, Dordrecht, 1991).
- [31] F. Natterer, *The Mathematics of Computerized Tomography* (Wiley, Chichester, 1986).
- [32] P. M. Morse and H. Feshbach, *Methods of Theoretical Physics* (McGraw-Hill, New York, 1953).
- [33] P. M. Morse and K. U. Ingard, *Theoretical Acoustics* (Princeton University Press, Princeton, 1968).
- [34] A. Louis and E. Quinto, in *Surveys on Solution Methods for Inverse Problems* (Springer, Vienna, 2000), pp. 147–154.
- [35] G. Ambartsoumian and S. K. Patch, eprint ArXiv:math.NA/0510638 (unpublished).